Supplementary Information

Supplementary Figure 1. Data stream for V892 Tau observed with the GBT. The raw signal is plotted against observation sequence number, in the four sub-bands of the 26-40 GHz receiver. Errors on the individual data points range from 0.2-1.0 mJy, with highest uncertainty at higher frequencies where the sky is more opaque. The co-added signals in each band have errors of 0.15-0.17 mJy (Supplementary Table 1), with different methods of weighting the points affecting these means by ≤0.05 mJy.

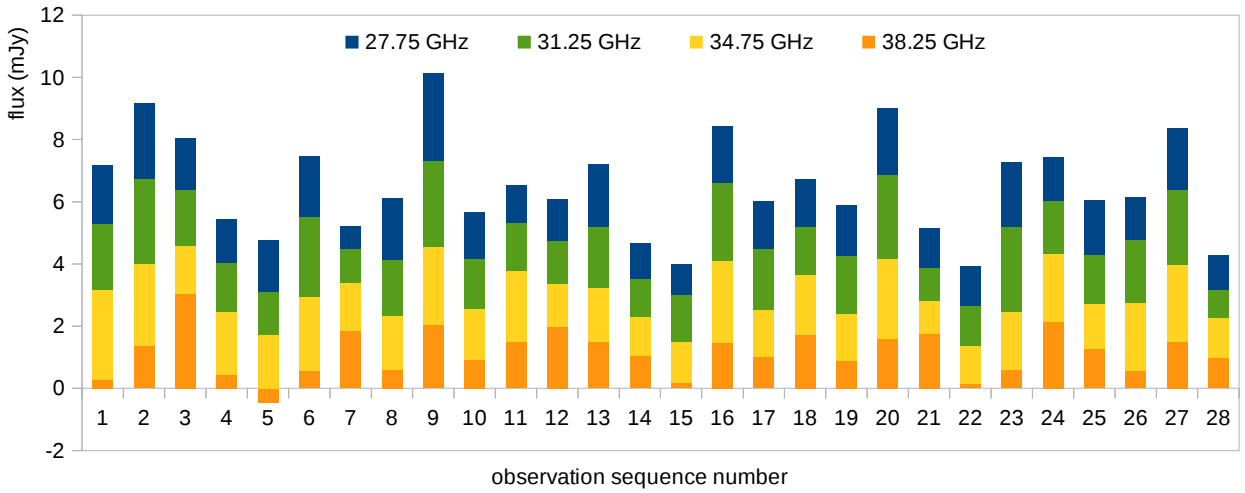

Supplementary Figure 2. GBT image of MWC 297 at 72 GHz. The pixel sizes are 2 arcsec and the beam size is shown by the circle. The time-stream data were filtered to remove sky and instrument effects, re-gridded into RA,Dec., and smoothed for clarity with an 8 arcsec wide Gaussian profile. The noise increases on the edge of the map and as a function of radius within the map due to the daisy-scanning mapping pattern. The radii of the areas sampled in the scan pattern were 0.8-1.0 arcmin.

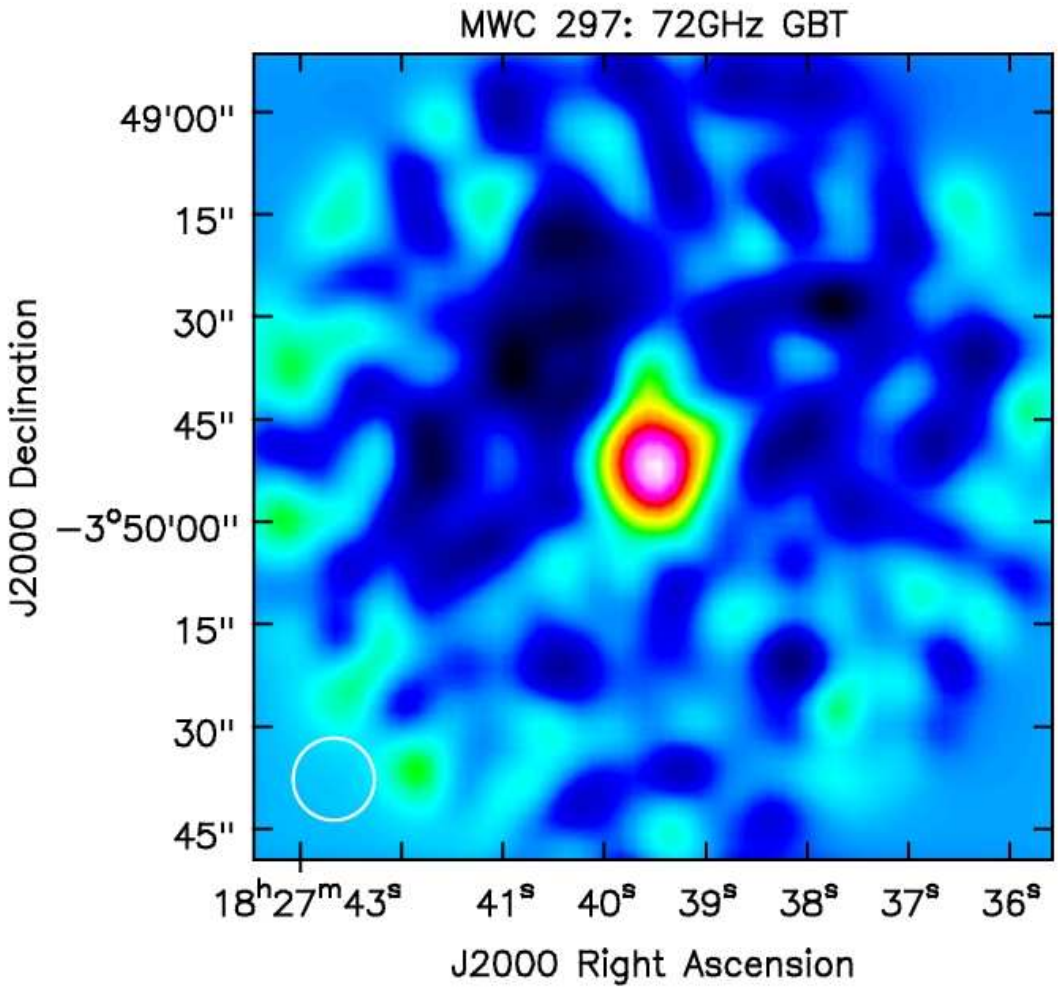

Supplementary Figure 3. Total flux (on log scale) against frequency for each AME system. Archival and literature data are shown with small circle symbols, with large circles showing the new flux results (Supplementary Table 1). Upper limits (2σ) are shown by triangles. Error bars are 1σ, and are set to minimum levels of 10% of measured flux, to account for uncertainties in calibration scales. The green dotted curves show the fits for combined wind and dust emission.

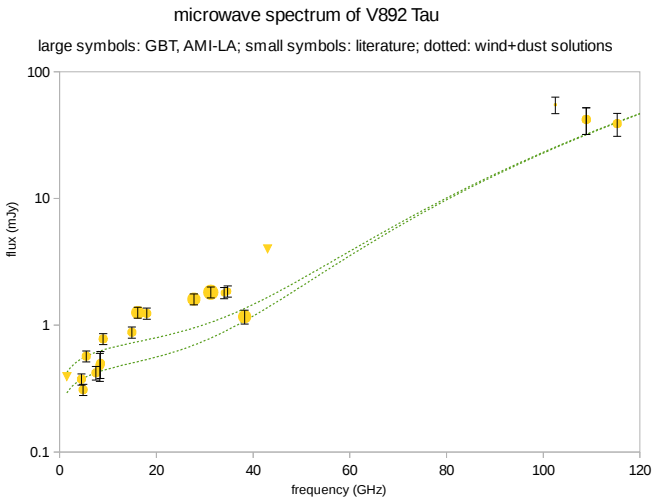

(Top:) V892 Tau. The dust component is fitted as a ν^4 power-law spectrum scaled to 22 mJy at 100 GHz; smaller dust indices produce negative residuals at frequencies around 40 GHz. The low-resolution measurement at 102.5 GHz (smallest symbol) was excluded from the fit, as the anomalously high flux may include material outside the dust disc. The wind component is 0.27 $\nu_{GHz}^{0.23}$ mJy in the lower curve, and varies by +45% in the upper curve[20,35].

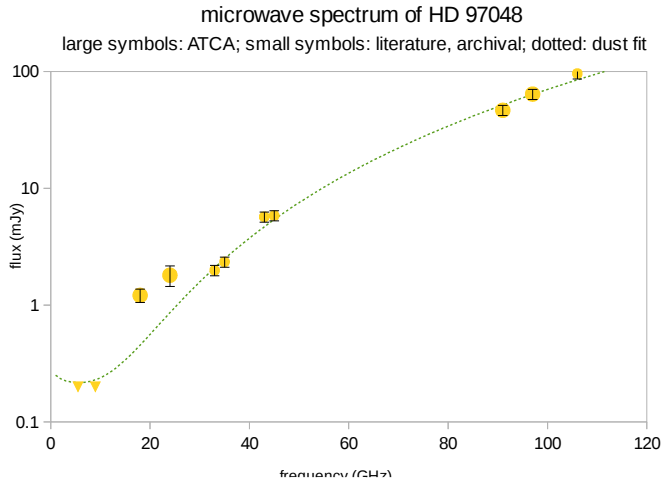

(Middle:) HD 97048. The dust is fitted with a $\nu^{3.25}$ spectrum, scaled to 70 mJy at 100 GHz. This fit demonstrates negligible AME at frequencies above 33 GHz; higher dust spectral indices are possible, yielding greater AME. A wind component with a 0.25 $\nu_{GHz}^{-0.1}$ mJy spectrum has been added, improving the fit at the limits set by the 2σ lowest-frequency data points.

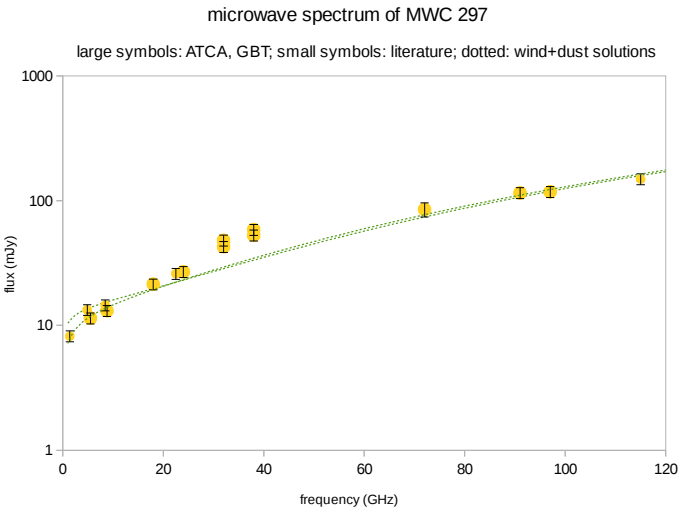

(Bottom:) MWC 297. The dust component is fitted as a ν^2 power-law spectrum, scaled to 127 mJy at 100 GHz. The fit assumes negligible AME at frequencies ≥72 GHz; relaxing this to higher frequency yields fits with more AME. The wind was fitted from our 5.5 and 8.8 GHz data with a $\nu^{0.28}$ power-law, while prior results at 4.9 and 8.4 GHz yielded a $\nu^{0.16}$ dependence. The two curves show these different cases when added to the dust signal (with the wind contributing 17-20% of the total signal at 100 GHz).

Supplementary Figure 3, continued. Systems without AME detections. Fits are illustrative, and not intended to account for higher-frequency dust measurements or time-variable wind emission discussed in the literature. New flux measurements are listed in Supplementary Table 2.

Sub-plots (a) to (d): GBT sample, with additional literature fluxes (small symbols).
(a) AB Aur: $\nu^{3.02}$ dust spectrum scaled to 9.2 mJy at 100 GHz plus constant 0.12 mJy wind flux.
(b) IC 2087 IR: $\nu^{1.25}$ wind spectrum scaled to 32 μJy at 1 GHz; negligible dust.
(c) SR 21: fit to lowest wind limits (dot-dashed line) with $\nu^{3.4}$ dust of 5.0 mJy at 100 GHz, plus constant 25 μJy wind; alternative fit to wind detections (dotted line) and neglecting limits, i.e assuming wind levels may vary with time, with $\nu^{2.9}$ dust, 4.8 mJy at 100 GHz, 40 μJy wind.
(d) T Tau: $\nu^{4.0}$ dust, 30 μJy at 100 GHz, constant 11 mJy wind (but strongly time variable).

Sub-plots (e) to (k): ATCA sample, with supplementary ATCA fluxes[46] for HD 100546.
(e) CD-42 11721: $\nu^{0.7}$ wind spectrum scaled to 0.4 mJy at 1 GHz; negligible dust, using the detections only, as the region is confused by multiple sources, and no single-object fit is possible.
(f) HD 34282: $\nu^{2.0}$ dust, 4.8 mJy at 100 GHz, constant 50 μJy wind.
(g) HD 95881: maximised model fitted to limits, $\nu^{0.6}$ wind spectrum scaled to 40 μJy at 1 GHz.
(h) HD 100453: maximised model fitted to limits, $\nu^{0.8}$ wind spectrum scaled to 25 μJy at 1 GHz.
(i) HD 100546: $\nu^{2.7}$ dust spectrum scaled to 58 mJy at 100 GHz plus constant 0.5 mJy wind flux.
(j) HD 139614: $\nu^{4.0}$ dust spectrum, 0.36 mJy at 100 GHz, $\nu^{0.65}$ wind spectrum, 70 μJy at 1 GHz.
(k) HD 169142: $\nu^{4.0}$ dust spectrum, 10.5 mJy at 100 GHz, $\nu^{0.35}$ wind spectrum, 100 μJy at 1 GHz.

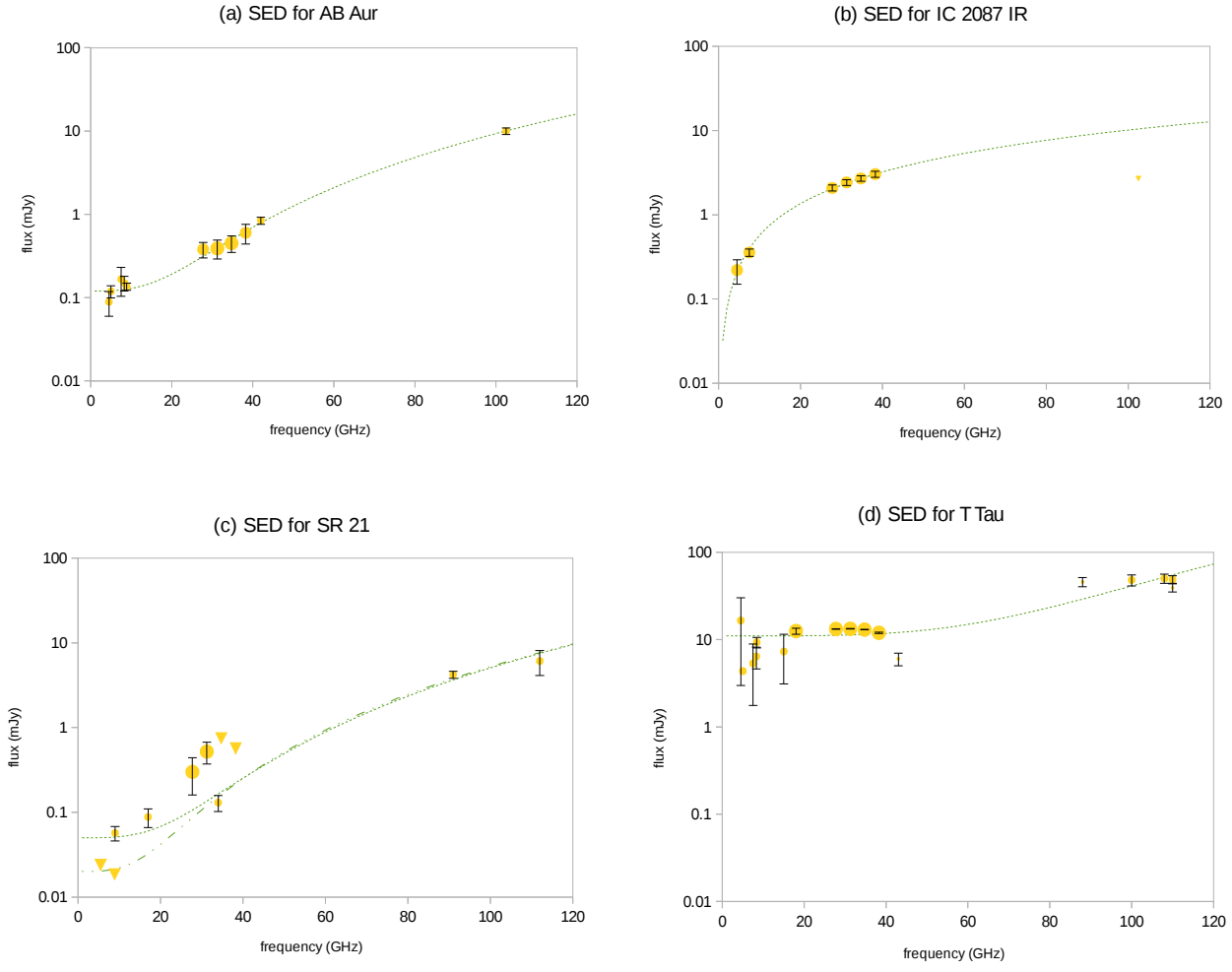

(e) SED for CD-42 11721

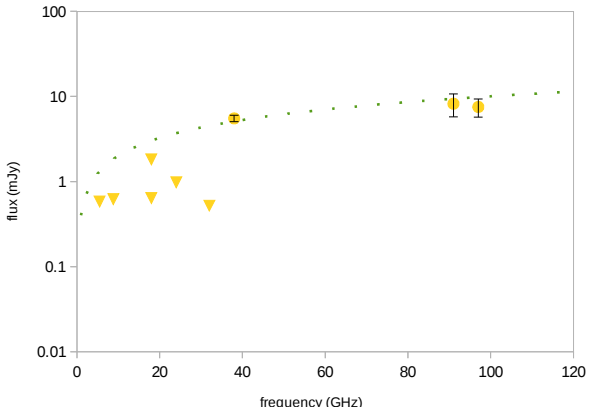

(f) SED for HD 34282

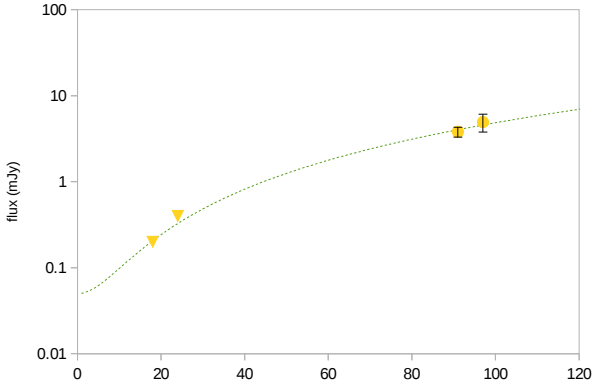

(g) SED for HD 95881

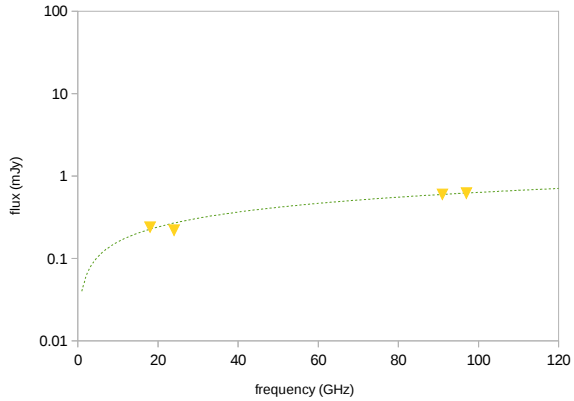

(h) SED for HD 100453

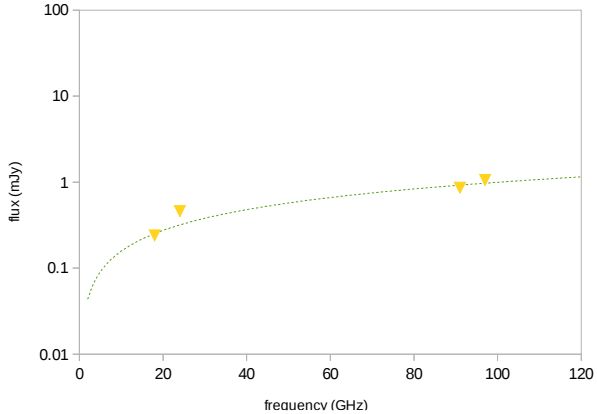

(i) SED for HD 100546

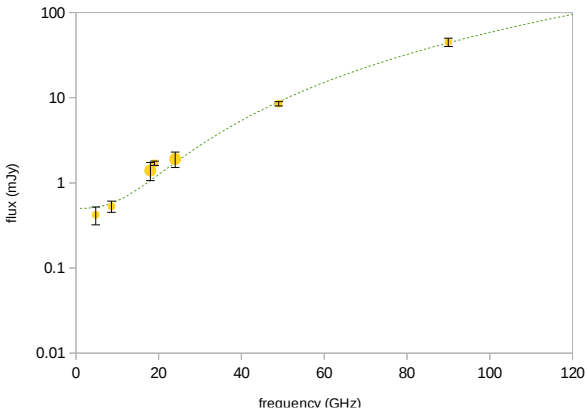

(j) SED for HD 139614

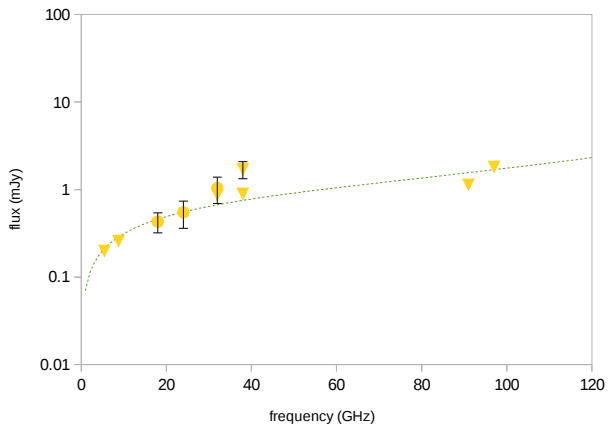

(k) SED for HD 169142

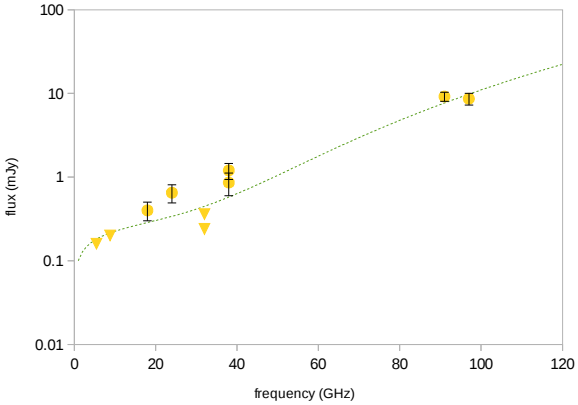

Supplementary Figure 4: *ISO-SWS* spectra towards the three diamond-hosting discs. For clarity, the V892 Tau data were binned over four 0.3 nm spectral channels, and 60 Jy was subtracted across the band for MWC 297. The nano-diamond peak wavelengths vary by ~±1 nm although this is near the limit of the spectral resolution; these shifts could indicate temperatures differences of ~100 K, within the ~800-1400 K range where hydrogenated nano-diamonds are stable[7,42].

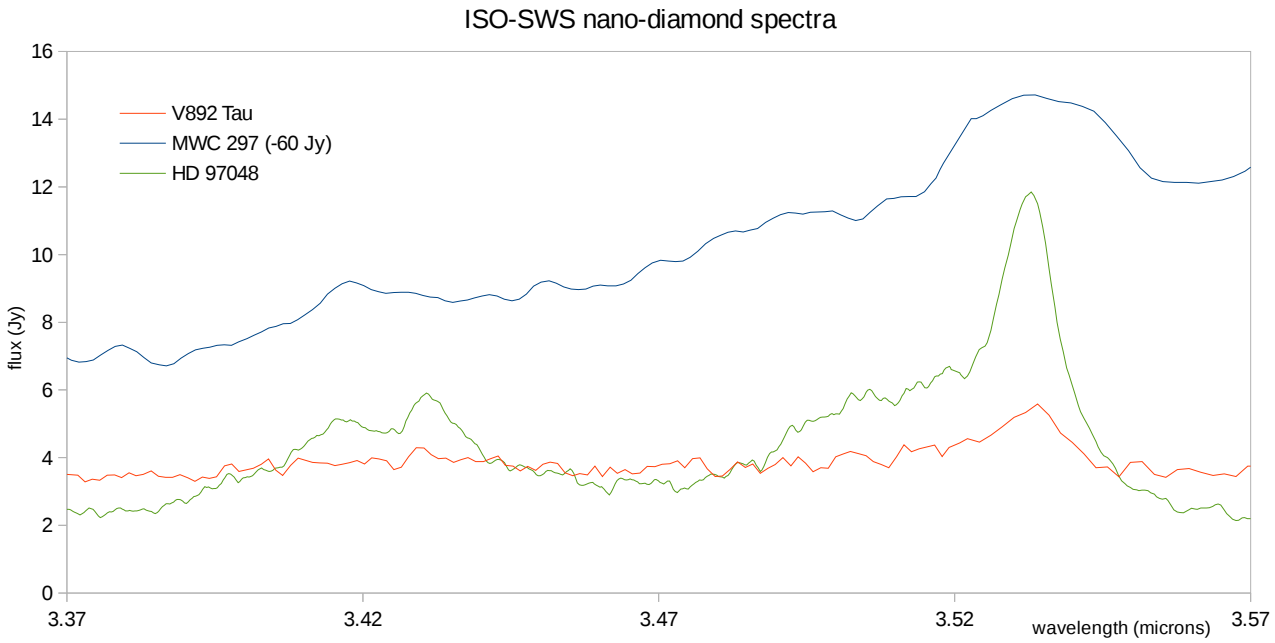

Supplementary Figure 5: Spectra from *Spitzer-IRS* (or *ISO-SWS* where not observed by *Spitzer*) showing the PAH features around 6.2 μm, for all the Herbig Ae stars observed within our sample (AME-detected objects shown with thick curves).

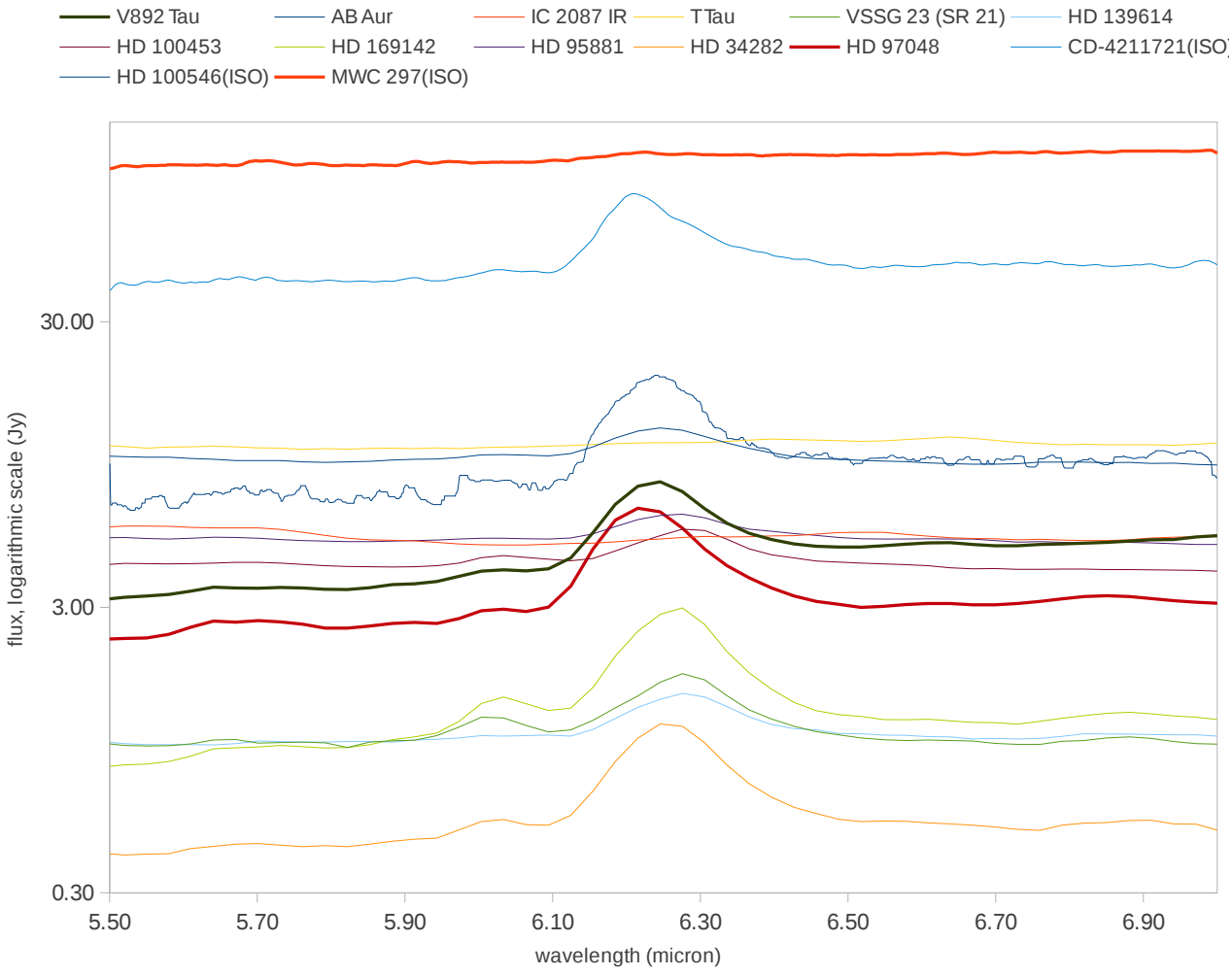

Supplementary Figure 6. Comparison of flux between the AME and nano-diamond 3.53 micron feature (left panel) and PAH 6.2 micron feature (right panel). The systems with detected AME are shown by the large blue circle symbols. In the comparison systems (shown with small yellow circles) AME upper limits are < 1.5 x 10^{-19} W m^{-2} and the nano-diamond fluxes are < 100 x 10^{-16} W m^{-2}. There is no such distinction for the PAH signal, i.e. there are systems without AME whose PAH line flux is higher than the AME-systems V892 Tau and HD 97048.

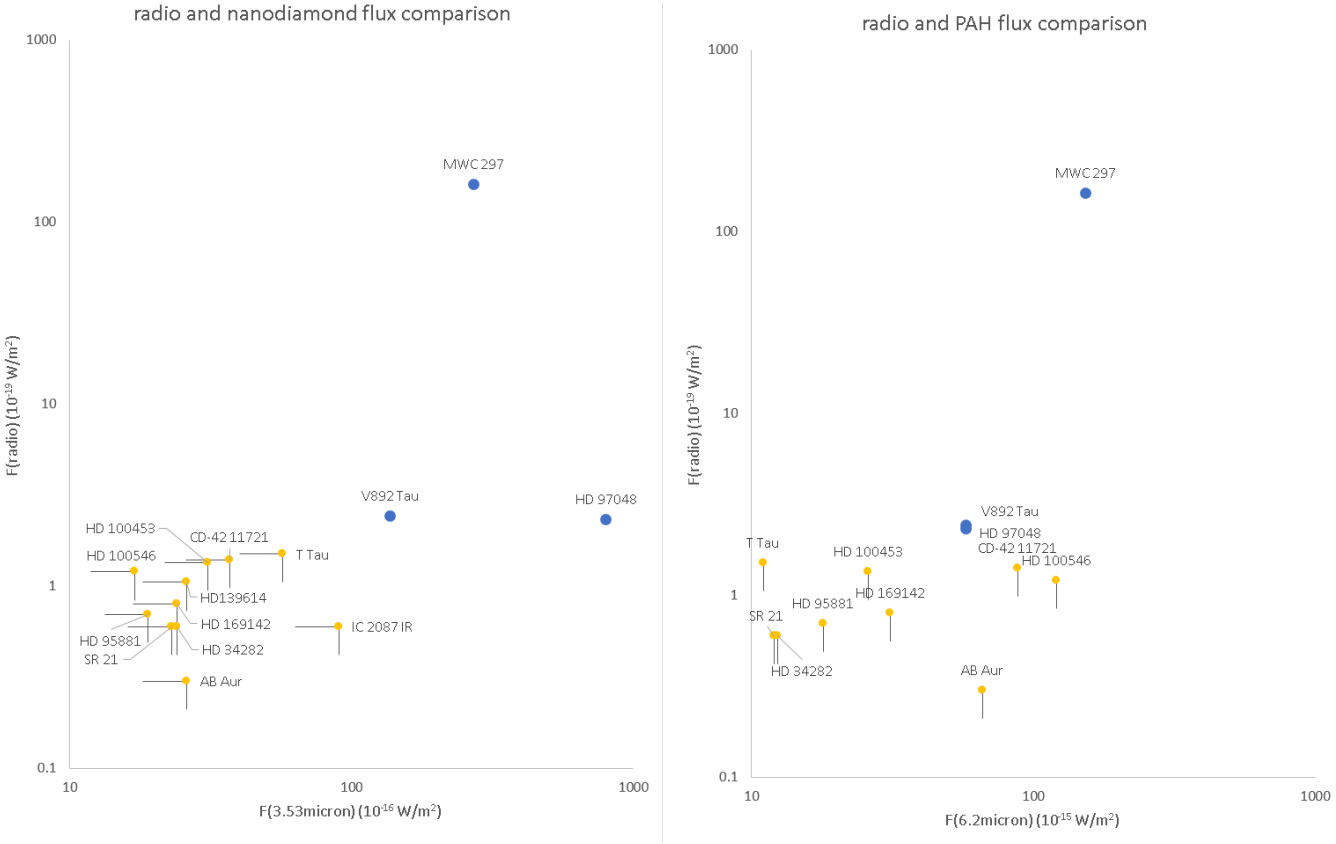

Supplementary Table 1. Results of observations of the sources with AME, from interferometry with ATCA, AMI-LA and ALMA, plus photometry with GBT[47]. The flux errors quoted are from the rms noise in the measurements, with error in fitting a point source model added in quadrature where appropriate, but excluding calibration uncertainties (which are incorporated in errorbars in Fig. S3). Upper limits are 2-sigma, the same confidence level as adopted for the literature data in Fig. S3. Fluxes marked (p) or (s) indicate use of the primary or secondary calibrator.

flux densities (mJy)	V892 Tau	MWC 297	HD 97048	HD 97048 (archival data)
F(5.5 GHz) (ATCA)		11.44 ± 0.24	≤ 0.2	
F(8.8 GHz) (ATCA)		13.11 ± 0.24	≤ 0.2	
F(16.1 GHz) (AMI-LA)	1.26 ± 0.05			
F(18 GHz) (ATCA)		21.40 ± 0.11 (s)	1.21 ± 0.16 (s)	
F(24 GHz) (ATCA)		26.86 ± 0.10 (s)	1.80 ± 0.36 (s)	
F(27.75 GHz) (GBT)	1.61 ± 0.15			
F(31.25 GHz) (GBT)	1.82 ± 0.17			
F(32 GHz) (ATCA)		42.71 ± 0.58 (s) 48.11 ± 0.62 (p)		
F(33 GHz) (ATCA)				2.0 ± 0.1
F(34.75 GHz) (GBT)	1.85 ± 0.17			
F(35 GHz) (ATCA)				2.3 ± 0.1
F(38 GHz) (ATCA)		52.8 ± 4.9 (s) 58.6 ± 0.9 (p)		
F(38.25 GHz) (GBT)	1.17 ± 0.15			
F(43 GHz) (ATCA)				5.7 ± 0.3
F(45 GHz) (ATCA)				5.8 ± 0.3
F(72 GHz) (GBT)		85 ± 11		
F(91 GHz) (ATCA)		115.4 ± 2.2 (p)	46.5 ± 3.8 (p)	
F(97 GHz) (ATCA)		117.8 ± 6.5 (p)	64.0 ± 6.0 (p)	
F(106 GHz) (ALMA)				96 ± 3

Supplementary Table 2. New flux measurements for sources without AME. F_x indicates flux in mJy at x GHz; multiple values indicate different calibrators. Errors for ATCA include the rms noise and point-source model fit uncertainty added in quadrature. Limits are 2σ, as in Supplementary Table 1.

source	facility	flux data
AB Aur	GBT	$F_{27.75} = 0.38 \pm 0.08$, $F_{31.25} = 0.39 \pm 0.10$, $F_{34.75} = 0.45 \pm 0.10$, $F_{38.25} = 0.60 \pm 0.16$
IC 2087 IR	GBT	$F_{27.75} = 2.08 \pm 0.17$, $F_{31.25} = 2.42 \pm 0.19$, $F_{34.75} = 2.70 \pm 0.20$, $F_{38.25} = 3.04 \pm 0.25$
SR 21	GBT	$F_{27.75} = 0.30 \pm 0.14$, $F_{31.25} = 0.52 \pm 0.15$, $F_{34.75} = 0.37 \pm 0.25$, $F_{38.25} = 0.18 \pm 0.19$
T Tau	GBT	$F_{27.75} = 13.21 \pm 0.11$, $F_{31.25} = 13.26 \pm 0.11$, $F_{34.75} = 13.00 \pm 0.12$, $F_{38.25} = 11.95 \pm 0.21$
CD-42 11721	ATCA	$F_{5.5} \leq 0.58$, $F_{8.8} \leq 0.62$, $F_{18} \leq 0.64$,1.82, $F_{24} \leq 0.98$, $F_{32} \leq 0.52$, $F_{38} = 5.52 \pm 0.47$, $F_{91} = 8.22 \pm 2.45$, $F_{97} = 7.53 \pm 1.82$
HD 34282	ATCA	$F_{18} \leq 0.20$, $F_{24} \leq 0.40$, $F_{91} = 3.81 \pm 0.50$, $F_{97} = 4.94 \pm 1.15$
HD 95881	ATCA	$F_{18} \leq 0.24$, $F_{24} \leq 0.22$, $F_{91} \leq 0.60$, $F_{97} \leq 0.62$
HD 100453	ATCA	$F_{18} \leq 0.24$, $F_{24} \leq 0.46$, $F_{91} \leq 0.86$, $F_{97} \leq 1.06$
HD 100546	ATCA	$F_{18} = 1.40 \pm 0.34$, $F_{24} = 1.91 \pm 0.39$
HD 139614	ATCA	$F_{5.5} \leq 0.20$, $F_{8.8} \leq 0.26$, $F_{18} = 0.43 \pm 0.11$, $F_{24} = 0.55 \pm 0.19$, $F_{32} = 1.04 \pm 0.35$, ≤ 0.88, $F_{38} = 1.71 \pm 0.38$, ≤ 0.90, $F_{91} \leq 1.14$, $F_{97} \leq 1.82$
HD 169142	ATCA	$F_{5.5} \leq 0.16$, $F_{8.8} \leq 0.20$, $F_{18} = 0.40 \pm 0.10$, $F_{24} = 0.65 \pm 0.16$, $F_{32} \leq 0.36$, ≤ 0.24, $F_{38} = 1.20 \pm 0.26$, 0.86 ± 0.26, $F_{91} = 9.18 \pm 1.16$, $F_{97} = 8.65 \pm 1.38$

Supplementary Table 3. Sample results and parameters (AME-systems in bold, top row). The second row lists AME flux in units of 10^{-19} W m^{-2}. AME limits were estimated from areas under a quasi-triangular spectrum, with a base ≤30 GHz wide, by a height of the greater of twice the maximum offset above the dust-plus-wind fit or twice the largest rms in the frequency range 18-38 GHz. The third row lists flux or 5σ limit (a conservative choice reflecting ground versus space discrepancies) for the 3.53 μm nano-diamond feature[16], in 10^{-16} W m^{-2}, with our derived ground, *ISO* estimates marked *, # respectively. The fourth row lists fluxes in the same unit estimated for the PAH 6.2 micron feature with *Spitzer*[6] or *ISO*[16]*;* our *Spitzer*-archive estimates are marked † and are uncertain for IC 2087 IR and T Tau where the feature may be a blend. The last three rows list literature estimates of distances (in pc); stellar luminosities (solar units) to facilitate comparison with L_{radio}, L_{IR}; and stellar effective temperatures (in K). L* estimates[12] have not been corrected for refinements in T_{eff} values[48] nor do they take into account new parallaxes from *GAIA* (in data release 1); *GAIA* distance estimates are noted in brackets, in cases of major change only.

	AB Aur	CD-42 11721	HD 34282	HD 95881	**HD 97048**	HD 100453	HD 100546	HD 139614	HD 169142	IC 2087 IR	**MWC 297**	SR 21	T Tau	**V892 Tau**
F_{AME}	≤ 0.3	≤ 1.4	≤ 0.6	≤ 0.7	2.3	≤ 1.4	≤ 1.2	≤ 1.1	≤ 0.8	≤ 0.6	160	≤ 0.6	≤ 1.5	2.4
$F_{3.53}$	≤ 26	≤ 37	≤ 24	≤24	800	≤ 31	≤ 17	≤ 26	≤ 24	≤ 90*	270	≤ 23*	≤ 57#	140
$F_{6.2}$	660	880	120	180†	580	260	1210	70	310	~90†	1540	120†	~110†	580
d	139	>136? (>1000)	~350	170 (935)	158	122 (243)	97	142	145	140	250	120	148	142
L*	60	~1x10^4	14	27	40	14	24	9	11	~72	~2x10^4	6	~17	80
T_{eff}	9800	~14000	9500	10000	10500	7250	9750	7750	7500	?	24500	5950	?	11200

Supplementary References

46. Wright, C. M. *et al.*, Resolving structure of the disk around HD100546 at 7 mm with ATCA. *Mon. Not. Roy. Astron. Soc.* **453**, 414-438 (2015).
47. Mason, B. S. *et al.*, A 31 GHz survey of low-frequency selected radio sources. *Astrophys. J.* **704**, 1433-1447 (2009).
48. Fairlamb, J. R.,Oudmaijer, R. D., Mendigutía, I., Ilee, J. D. & van den Ancker, M. E. A spectroscopic survey of Herbig Ae/Be stars with X-shooter - I. Stellar parameters and accretion rates. *Mon. Not. Royal Astron. Soc.* **453**, 976-1001 (2015).